



# Flow-induced oscillations of a transversely buckled flexible filament

Zepeng Chen<sup>1,2</sup>, Yingzheng Liu<sup>1</sup>  and Hyung Jin Sung<sup>2</sup> 

<sup>1</sup>Key Laboratory of Education Ministry for Power Machinery and Engineering, School of Mechanical Engineering, Shanghai Jiao Tong University, 800 Dongchuan Road, Shanghai 200240, PR China

<sup>2</sup>Department of Mechanical Engineering, KAIST, 291 Daehak-ro, Yuseong-gu, Daejeon 34141, Korea

**Corresponding author:** Hyung Jin Sung, [hjsung@kaist.ac.kr](mailto:hjsung@kaist.ac.kr)

(Received 25 July 2024; revised 3 December 2024; accepted 22 December 2024)

---

The flow-induced oscillation of a transversely clamped buckled flexible filament in a uniform flow was explored using the penalty immersed boundary method. Both inverted and conventional configurations were analysed. The effects of bending rigidity, filament length and Reynolds number were examined. As these parameters were varied, four distinct modes were identified: conventional transverse oscillation mode, deflected oscillation mode, inverted transverse oscillation mode and structurally steady mode. The filament exhibited a 2S wake pattern under the conventional transverse oscillation mode and the small-amplitude inverted transverse oscillation mode, a P wake pattern under the deflected oscillation mode and a 2S + 2P wake pattern for the large-amplitude inverted transverse oscillation mode. Irrespective of their initial conditions, all of the filaments converged to the conventional transverse oscillation mode under low bending rigidity. Multistability was observed in the transversely clamped buckled flexible filament under moderate bending rigidity. The deflection in the oscillation mode increased with increasing filament length. The inverted buckled filament was sensitive to the Reynolds number, unlike the conventional buckled filament. The transverse oscillation mode demonstrated superior energy-harvesting performance.

**Key words:** flow–structure interactions

---

## 1. Introduction

Clean energy has become a focal point, praised for its eco-friendliness and cost effectiveness in contrast to traditional fossil fuels. Flexible structures such as flags and

sails can effectively convert fluid kinetic energy into electric energy by incorporating piezoelectric materials on their surfaces, thus holding potential for energy harvesting. Buckled filaments, clamped on both ends, possess substantial elastic energy in their initial configuration. The substantial deflection and high strain energy of buckled filaments make them suitable for energy-harvesting applications. Hence, understanding the flow-induced oscillation of buckled flexible filaments is critical for advancing the field of flexible energy harvesting.

Flags, or filaments, are ubiquitous flexible structures whose flow-induced vibration has been extensively studied through various theoretical, experimental and numerical methods. Categorized on the basis of clamping conditions, flags can be conventional, inverted or wall clamped. A conventional flag features a clamped leading edge and a free trailing edge, exhibiting stretched-straight, flapping and chaos modes as parameters such as the mass ratio, Reynolds number and bending rigidity vary (Zhang *et al.* 2000; Zhu & Peskin 2003; Shelley, Vandenberghe & Zhang 2005; Alben & Shelley 2008; Michelin, Llewellyn Smith & Glover 2008; Banerjee, Connell & Yue 2015; Cisonni *et al.* 2017). Instability in conventional flags arises from the interplay between pressure and elastic forces (Eloy *et al.* 2008; Shelley & Zhang 2011), with a relatively high critical velocity required to activate oscillation modes, limiting their application in energy harvesting (Doaré & Michelin 2011; Michelin & Doaré 2013; Xia, Michelin & Doaré 2015; Yu & Liu 2016). Kim *et al.* (2013) introduced inverted flags, which are clamped at the trailing edge, reducing the critical flow velocity. Various modes, including straight, flapping, deflected, deflected flapping and chaos modes, emerge in inverted flags as the mass ratio, Reynolds number and bending rigidity vary (Gurugubelli & Jaiman 2015; Tang, Liu & Lu 2015; Sader *et al.* 2016; Orrego *et al.* 2017; Yu, Liu & Chen 2017). For lightweight flags, flapping results from vortex-induced vibration (Sader *et al.* 2016; Sader, Huertas-Cerdeira & Gharib 2016); by contrast, heavy flags exhibit self-induced vibration (Goza, Colonius & Sader 2018; Tavallaeinejad *et al.* 2020). Despite their potential for energy harvesting due to large oscillation amplitudes, inverted flags are applicable only within specific ranges of flow speeds and bending rigidity (Ryu *et al.* 2015; Park *et al.* 2016). The motion of vertically wall-clamped flags, where clamping is perpendicular to the flow direction, has also been investigated (Lee *et al.* 2017, 2018; Chen *et al.* 2020a, 2020b; Park 2020); the oscillation amplitudes of such flags are typically lower than those of inverted and conventional flags, making them less suitable for energy harvesting. Using elastic energy for energy harvesting requires careful consideration of material properties. Several methods can convert stored elastic energy into electricity, including piezoelectric (Jung & Yun 2010; Cottone *et al.* 2012), electromagnetic (Bai *et al.* 2022) and triboelectric mechanisms (Zhu & Zu 2013; Kim *et al.* 2020).

The buckled filament, characterized by its two clamped edges, stores greater elastic energy than a single-side-clamped filament. Its bistability enables it to snap through from one equilibrium state to another under external excitation, resulting in substantial deflection (Gomez, Moulton & Vella 2017a; Gomez, Moulton & Vella 2017b). Kim *et al.* (2020) proposed energy harvesting based on the flow-induced snap-through oscillation of streamwise-clamped buckled sheets, investigating its instability mechanism experimentally (Kim *et al.* 2021; Kim, Kim & Kim 2021). Mao, Liu & Sung (2023) systematically examined the effect of Reynolds number, bending rigidity and filament length on the snap-through dynamics. They delineated distinct phenomena, including snap-through oscillation (STO), streamwise oscillation and structurally steady modes. The critical bending rigidity to activate STO is relatively lower than that observed in inverted flags. Efforts have been made to enhance the critical bending rigidity of STO, with Chen *et al.* (2023) exploring the effect of the edge condition. They found that a

simply supported leading edge combined with a clamped trailing edge led to increased critical bending rigidity and improved energy-harvesting performance. Moreover, buckled filaments performed better in channel flow conditions, exhibiting higher bending rigidity (Chen *et al.* 2024). For a side-by-side configuration, an appropriate gap distance between filaments can enhance energy-harvesting performance and increase critical bending rigidity (Chen, Liu & Sung 2024). Despite these efforts, the critical bending rigidity of buckled filaments remains lower than that of conventional and inverted flags because of the substantial external energy required to initiate snap through (Chen *et al.* 2023).

To address this challenge, transversely clamped buckled filaments, with clamped edges perpendicular to the flow, have been proposed to expand their application area. Transversely clamped buckled filaments, which combine the high critical bending rigidity of inverted flags with the high strain energy of buckled filaments, have emerged as a more suitable candidate for energy harvesting. In the present investigation into the dynamics of transversely buckled flexible filaments, bending rigidity emerges as the pivotal parameter. Understanding the fluid dynamics associated with variations in bending rigidity is essential. Experimentally manipulating bending rigidity is highly challenging, mainly because of the difficulty in sourcing appropriate materials. Employing numerical analysis significantly facilitates the research process and offers advantages over experimentation for parametric and quantitative analyses of fluid–flexible structure interactions. In particular, the immersed boundary (IB) method has been widely adopted to handle this interaction (Huang, Shin & Sung 2007; Huang & Sung 2010; Huang, Chang & Sung 2011; Ryu *et al.* 2015; Park, Ryu & Sung 2019). Few numerical studies on flow-induced oscillations of transversely clamped buckled filaments have been reported. More importantly, the mechanisms underlying the energy-harvesting efficiency of these filaments have not yet been fully elucidated and warrant a more detailed investigation.

The objective of the present study is to explore the flow-induced oscillations of transversely clamped buckled flexible filaments using the penalty IB method. We investigate two distinct configurations: inverted and conventional buckled filaments. The effects of bending rigidity ( $\gamma$ ), filament length ( $L$ ) and Reynolds number ( $Re$ ) on mode transition are examined for both configurations. When these parameters are varied, four distinct modes are identified: conventional transverse oscillation ( $TO_c$ ) mode, deflected oscillation (DO) mode, inverted transverse oscillation ( $TO_i$ ) mode and structurally steady (SS) mode. The corresponding wake patterns and filament motions for each mode are analysed. To elucidate the relationship between the filament's oscillation and vortex shedding, we examine vorticity and pressure contours while tracking the temporal evolution of force and energy. Finally, we evaluate the energy-harvesting performance of inverted and conventional buckled filaments using elastic energy and power coefficient metrics.

## 2. Computational model

### 2.1. Problem formulation

The transversely clamped filament can be categorized into two types: inverted and conventional buckled filaments. Schematics illustrating their configurations in a uniform flow are depicted in figures 1(a) and 1(b), respectively. In these schematics,  $L_0$  represents the distance between the two clamped edges and  $L$  denotes the length of the filament. The fluid motion is described within a fixed Euler coordinate system, and  $x$  and  $y$  represent the streamwise and transverse directions, respectively. Dirichlet boundary conditions ( $u = U_0$ ,  $v = 0$ , where  $u$  is the velocity component in the  $x$ -direction,  $v$  is the velocity component in

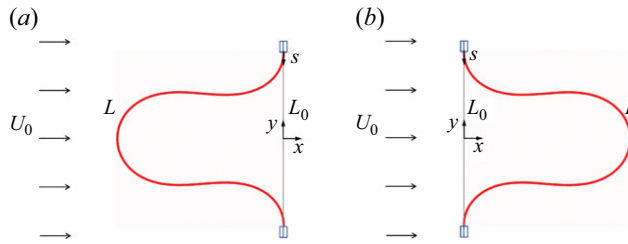


Figure 1. Schematic of the (a) inverted and (b) conventional buckled flexible filament in a uniform flow.

the  $y$ -direction and  $U_0$  represents the free-stream inflow velocity) are applied at the inlet, top and bottom boundaries, whereas a Neumann-type boundary condition ( $\partial \mathbf{u} / \partial x = 0$ ) is enforced at the outlet (Huang & Sung 2007). The filament's motion is defined within a moving curvilinear coordinate system ( $s$ ), where  $s$  represents the arc length of the filament. The clamped edges are indicated by boxes, positioned at  $(0, 0.5)$  and  $(0, -0.5)$ . The initial buckled shape is determined via simulation in a static fluid environment, starting from an arc-shaped configuration. During the process, the filament's elastic force equilibrates with the fluid force.

The fluid motion is governed by the Navier–Stokes equations and the continuity equation, whose non-dimensional forms are

$$\frac{\partial \mathbf{u}}{\partial t} + \mathbf{u} \cdot \nabla \mathbf{u} = -\nabla p + \frac{1}{Re} \nabla^2 \mathbf{u} + \mathbf{f}, \quad (2.1)$$

$$\nabla \cdot \mathbf{u} = 0, \quad (2.2)$$

where  $\mathbf{u} = (u, v)$  is the fluid velocity vector,  $p$  is the pressure and  $\mathbf{f} = (f_x, f_y)$  represents the momentum forcing used to enforce the no-slip condition along the IB; the Reynolds number  $Re$  is defined as  $\rho_0 U_0 L_0 / \mu$ , where  $\rho_0$  and  $\mu$  are the fluid density and the dynamic viscosity, respectively. Equations (2.1) and (2.2) are non-dimensionalized using the following characteristic scales:  $L_0$  for length,  $U_0$  for velocity,  $L_0 / U_0$  for time,  $\rho_0 U_0^2$  for pressure and  $\rho_0 U_0^2 / L_0$  for the momentum forcing  $\mathbf{f}$ . For convenience, the dimensionless quantities are written in the same form as their dimensional counterparts.

The filament motion is governed by the dimensionless nonlinear structure equation and the inextensibility condition

$$\frac{\partial^2 \mathbf{X}}{\partial t^2} = \frac{\partial}{\partial s} \left( T \frac{\partial \mathbf{X}}{\partial s} \right) - \gamma \frac{\partial}{\partial s} \left( \frac{\partial \mathbf{K}}{\partial s} \mathbf{n} \right) - \mathbf{F}_f, \quad (2.3)$$

$$\frac{\partial \mathbf{X}}{\partial s} \cdot \frac{\partial \mathbf{X}}{\partial s} = 1, \quad (2.4)$$

where  $\mathbf{X} = (X(s, t), Y(s, t))$  denotes the displacement vector of the filament,  $s$  is the arclength,  $T$  and  $\gamma$  represent the tension coefficient and bending rigidity along the filament, respectively,  $K$  is the curvature of the filament,  $\mathbf{n}$  denotes the normal direction and  $\mathbf{F}_f$  is the Lagrangian momentum forcing exerted by the surrounding fluid on the filament. Equations (2.3) and (2.4) are non-dimensionalized by the following characteristic scales:  $L_0$  for length,  $L_0 / U_0$  for time,  $\rho_1 U_0^2$  for the tension coefficient  $T$ ,  $\rho_1 U_0^2 L_0^2$  for the bending rigidity  $\gamma$  and  $\rho_1 U_0^2 / L_0$  for the Lagrangian forcing  $\mathbf{F}_f$ . Here,  $\rho_1$  denotes the density difference between the filament and the surrounding fluid. Given that the filament's cross-sectional length is negligible,  $\rho_1$  is treated as the filament's density. The elastic force

of the filament is given by  $\mathbf{F}_s = \partial/\partial s(T(\partial\mathbf{X}/\partial s)) - \gamma(\partial/\partial s)((\partial\mathbf{K}/\partial s)\mathbf{n})$ . In the present study,  $\gamma$  is a constant value during filament motion, whereas  $T$  is assumed to be a function of  $s$  and  $t$ , determined by the inextensibility. A Poisson equation is constructed to solve the value of  $T$  (Huang *et al.* 2007). Clamped boundary conditions are imposed at the two fixed edges of the filament, which are

$$\frac{\partial\mathbf{X}}{\partial s} = (0, -1) \quad \text{at } s = 0, L. \tag{2.5}$$

The penalty IB method is used to calculate the interaction between the filament and the fluid. In this approach, the IB represents the flexible structure’s interface, which is divided into a massive boundary and a massless boundary, interconnected by a stiff spring. The Lagrangian momentum forcing  $\mathbf{F}_f$  is calculated using the following equation (Goldstein, Handler & Sirovich 1993):

$$\mathbf{F}_f = \alpha \int_0^t (\mathbf{U}_{ib} - \mathbf{U})dt' + \beta(\mathbf{U}_{ib} - \mathbf{U}), \tag{2.6}$$

where  $\alpha = -3 \times 10^6$  and  $\beta = -100$  are large negative constants to impose the no-slip condition on the IB (Huang *et al.* 2007; Shin, Huang & Sung 2008). Although  $\alpha$  and  $\beta$  do not directly impact the filament’s motion, they affect system stability by limiting the maximum allowable time step. The time step must satisfy the condition  $-\alpha\Delta t^2 - 2\beta\Delta t < C_T$ , where  $C_T$  is a constant value related to  $\rho$ . Here,  $\mathbf{U}_{ib}$  is the velocity of the massless boundary obtained by interpolation at the IB, and  $\mathbf{U}$  denotes the velocity of the massive boundary, calculated as  $\mathbf{U} = d\mathbf{X}/dt$ . The transformation between Eulerian and Lagrangian variables is realized using the Dirac delta function. The values of  $\mathbf{U}_{ib}$  and  $\mathbf{f}$  can be obtained using the following equations:

$$\mathbf{U}_{ib}(s, t) = \int_{\Omega} \mathbf{u}(x, t) \delta(\mathbf{X}(s, t) - x)dx, \tag{2.7}$$

$$\mathbf{f}(x, t) = \rho \int_{\Gamma} \mathbf{F}_f(s, t) \delta(x - \mathbf{X}(s, t))ds, \tag{2.8}$$

where  $\rho = \rho_1/\rho_0 L_0 = 1$  is the density ratio derived from the non-dimensionalization process.

The elastic strain energy  $E_s$  is an important parameter for estimating the energy-harvesting performance of the filament; it is defined as

$$E_s(t) = \int_{\Gamma} 0.5\gamma K^2(s, t) ds. \tag{2.9}$$

To directly calculate the electricity generated during filament motion, we consider piezo–structure coupling. The filament is equipped with infinitesimal piezoelectric patches on both sides, each with segmentation lengths much smaller than  $L$ . These patches are connected to an electric circuit, which harnesses the piezoelectric effect: the stretching and compression of the patches induce charge transfer between each patch’s electrodes. An electric voltage applied to the electrodes creates additional internal torque on the piezoelectric patch and the filament (Doaré *et al.* 2011). Each patch’s local electric state is characterized by the voltage between its positive electrodes, denoted as  $V(s, t)$  and the charge transfer  $Q(s, t)$  along the filament axis. Both  $V(s, t)$  and  $Q(s, t)$  are continuous

functions of  $s$  and  $t$  (Michelin *et al.* 2013). The piezoelectric coupling effect is modelled by the following equations:

$$Q(s, t) = cV + \chi K, \tag{2.10}$$

$$M(s, t) = -\gamma K + \chi V, \tag{2.11}$$

where  $M(s, t)$  is the torque of the filament. The constants  $c$  and  $\chi$  are the lineic capacitance and piezoelectric coupling coefficient, respectively, which depend on the material and geometric properties of the patch pair (Doaré *et al.* 2011). The positive electrodes are linked to a purely resistive circuit with lineic conductivity, as depicted in the equation

$$\frac{\partial Q}{\partial t}(s, t) = -\zeta V, \tag{2.12}$$

where  $\zeta$  represents the linear conductivity coefficient between the piezoelectric patches on the upper and lower surfaces of the filament. When the piezoelectric effect is considered, the equivalent bending rigidity can be expressed as

$$\gamma_E = \frac{\partial M}{\partial s} = -\gamma \frac{\partial K}{\partial s} + \chi \frac{\partial V}{\partial s}. \tag{2.13}$$

By combining equations (2.10)–(2.13), we can express the nonlinear structure equation incorporating the piezoelectric effect and the electrical equation as follows:

$$\frac{\partial^2 \mathbf{X}}{\partial t^2} = \frac{\partial}{\partial s} \left( T \frac{\partial \mathbf{X}}{\partial s} \right) - \gamma \frac{\partial}{\partial s} \left( \frac{\partial K}{\partial s} \mathbf{n} \right) + \alpha_e \sqrt{\gamma} \frac{\partial}{\partial s} \left( \frac{\partial V}{\partial s} \mathbf{n} \right) - \mathbf{F}_f, \tag{2.14}$$

$$\beta_e \frac{\partial V}{\partial t} = -V - \alpha_e \beta_e \sqrt{\gamma} \frac{\partial K}{\partial t}, \tag{2.15}$$

where  $\alpha_e = \chi / \sqrt{c\gamma L}$  and  $\beta_e = cU / \zeta L$  are the coupling coefficient and the tuning coefficient of the electrical system, respectively (Shoele & Mittal 2016). Here,  $\gamma_L$  represents the dimensional bending rigidity of the filament. The voltage and charge density are non-dimensionalized by  $U\sqrt{\rho L}/c$  and  $U\sqrt{\rho Lc}$ , respectively. In the present study, we maintain  $\alpha_e$  and  $\beta_e$  at constant values of 0.1 and 0.1, respectively, without affecting the filament motion. The harvested energy, which is equivalent to the instantaneous power dissipated in the piezo patches (Michelin *et al.* 2013; Shoele *et al.* 2016), can be assessed using the power coefficient, defined as

$$c_p = \frac{P}{\rho U^3 L} = \frac{1}{\beta_e} \int_0^L V^2 ds. \tag{2.16}$$

The fractional step method on a staggered Cartesian grid is adopted to solve the Navier–Stokes equations (Kim, Baek & Sung 2002). A direct numerical method developed by Huang *et al.* (2007) is used to calculate the filament motion. Details of the discretization of the governing equations and numerical method can be found in the works of Kim, Sung & Hyun (1992) and Kim *et al.* (2002).

## 2.2. Validation

Table 1 summarizes the results of the domain test for the conventional buckled filament with  $L/L_0 = 3$ ,  $\gamma = 0.01$ ,  $Re = 100$ . The domain dimensions, defined by its length and

	Domain	$\overline{C}_D$	$\varepsilon_{\overline{C}_D}$	$A_y$	$\varepsilon_{A_y}$	$St$	$\varepsilon_{St}$
I	$32 \times 8$	1.4675	0.0598	0.8319	0.0452	0.1500	0.0714
	$32 \times 16$	1.3712	0.0097	0.8500	0.0244	0.1400	0
	$32 \times 24$	1.3847	–	0.8713	–	0.1400	–
	$16 \times 16$	–	–	–	–	–	–
II	$32 \times 16$	1.3712	0.0177	0.8500	0.0132	0.1400	0
	$64 \times 16$	1.3473	–	0.8389	–	0.1400	–

Table 1. Domain test, including the averaged drag coefficient  $\overline{C}_D$ , oscillation amplitude of  $A_y$ , the Strouhal number  $St$  and the relative errors  $\varepsilon$  to  $32 \times 24$  (domain height test in part I) and  $64 \times 16$  (domain length test in part II) ( $L/L_0 = 3$ ,  $\gamma = 0.01$ ,  $Re = 100$ , conventional configuration).

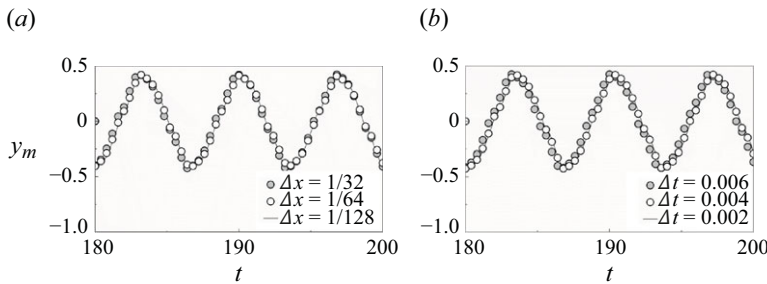


Figure 2. Time evolution of the transverse displacement of the mid-point of the filament ( $y_{um}$ ) for different (a) grid sizes and (b) time steps.

height, were specifically chosen to induce large-amplitude oscillations in the filament. The table includes the averaged drag coefficient  $\overline{C}_D$ , oscillation amplitude  $A_y$  and the Strouhal number  $St (= f_v L_0 / U_0)$ , along with the corresponding relative error  $\varepsilon$ . Here,  $f_v$  represents the vortex shedding frequency from the filament. The simulation does not converge for the  $16 \times 16$  domain. The results for the  $32 \times 16$  domain are consistent with those for the  $32 \times 24$  and  $64 \times 16$  domains. Therefore, a domain size of  $32 \times 16$  was selected, covering the range of  $-10L_0 \leq x \leq 22L_0$  and  $-8L_0 \leq y \leq 8L_0$ , as this allows for simulation over a greater number of time steps, thereby enhancing the accuracy of the results. To assess the impact of grid resolution and time step on the simulation outcomes, convergence studies were conducted for various grid resolutions and time steps. Figure 2 shows the time evolution of the transverse displacement at the midpoint of the filament. The results obtained with  $\Delta x = 1/64$  and  $\Delta t = 4 \times 10^{-4}$  align well with those for  $\Delta x = 1/128$  and  $\Delta t = 2 \times 10^{-4}$ . Consequently, a grid resolution of  $1/64$  and a time step of  $4 \times 10^{-4}$  were chosen to ensure sufficiently high accuracy in the simulation. The maximum Courant number was approximately 0.04 in the simulation. The grid was uniform in the  $x$ -direction but stretched in the  $y$ -direction. Specifically, within the range  $-Y/4 \leq y \leq Y/4$ , the grid size was  $\Delta y = \Delta x$ . Outside this range, the grid size was the grid size was  $\Delta y = 2\Delta x$ . The grid size for the filament was matched to that of the fluid domain.

We conducted an experiment to explore the dynamics of inverted buckled filaments. The experiments were carried out in a small open suction wind tunnel, with wind speeds ranging from 10 to 55  $\text{m s}^{-1}$ . The flexible filament used was made of polyethylene terephthalate (PET) film with a thickness ( $h$ ) of 0.1 mm, Young’s modulus ( $E$ ) of 4 GPa,

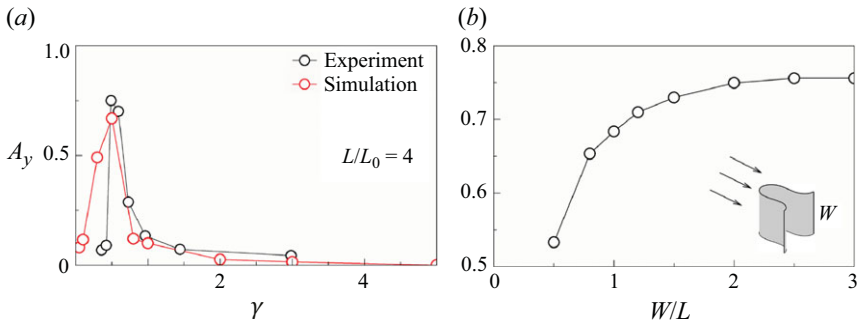


Figure 3. (a) Oscillation amplitude ( $A_y$ ) as a function of  $\gamma$  and (b)  $A_y$  as a function of aspect ratio ( $W/L$ ) under  $\gamma = 0.5$  ( $L/L_0 = 4$ ).

Poisson’s ratio ( $\sigma$ ) of 0.4, density of  $1.3 \times 10^3 \text{ kg m}^{-3}$ . In this study, we compared the effect of  $\gamma$  on the oscillation amplitude ( $A_y$ ) for both the experiment and the simulation with  $L/L_0 = 4$ , as shown in figure 3(a). In the experiment, the bending rigidity  $\gamma$  is defined as  $\gamma = B/\rho_0 U^2 L^3$ , where  $B = Eh^3/12(1 - \sigma)^2$  is the flexural rigidity of the filament (Kim *et al.* 2013). Both sets of results showed similar trends: the filament remains in a structurally steady mode at high  $\gamma$ , and as  $\gamma$  decreases below a certain threshold,  $A_y$  suddenly increases due to the transition to the deflected oscillation mode, where the filament oscillates with a bias towards one side. Further decreases in  $\gamma$  result in the filament becoming too soft to sustain the fluid force, leading to a reduction in  $A_y$ . Despite the differences in Reynolds numbers between the simulation ( $O(10^2)$ ) and the experiment ( $O(10^4)$ ), the overall trends are consistent, demonstrating that our simulation captures the physical phenomena of the inverted buckled filament. Figure 3(b) examines the effect of the aspect ratio ( $W/L$ ), where  $W$  is the spanwise length, on the oscillation amplitude ( $A_y$ ). As  $W/L$  increases beyond 2,  $A_y$  converges to a constant value, suggesting that the effect of  $W/L$  is negligible. This observation aligns with previous studies on conventional flags (Banerjee *et al.* 2015; Gurugubelli & Jaiman 2019). Experimental studies are limited by the difficulty of altering the parameters of filament materials, which constrains the scope of research. Simulations, however, are better suited for exploring a wide range of parameters and investigating additional phenomena in both inverted and conventional buckled filaments.

### 3. Results and discussion

#### 3.1. Modes of filament motion

In this section, we examine the motion of the transversely clamped filament across different modes. When  $L/L_0$  and  $\gamma$  vary, four distinct modes emerge: the SS mode, the  $TO_i$  mode, the DO mode and the  $TO_c$  mode. To facilitate the initiation of large oscillations, we selected a long filament ( $L/L_0 = 3$ ), allowing for an examination of the motion of the transversely buckled filament. Figure 4 illustrates the superposition of the filament’s instantaneous shapes in the SS,  $TO_i$ , DO and  $TO_c$  modes. Due to the bistable nature of the buckled filament, the transversely clamped filament can exhibit both conventional flag-like motion and inverted flag-like motion in the flow, depending on the initial conditions. Under high  $\gamma$ , the filament demonstrates resilience against unsteady fluid forces, manifesting the SS mode (depicted in figure 4(a) for the inverted initial state; the conventional initial state exhibits a reversed shape). The  $TO_i$  mode, reminiscent of the flapping mode observed in

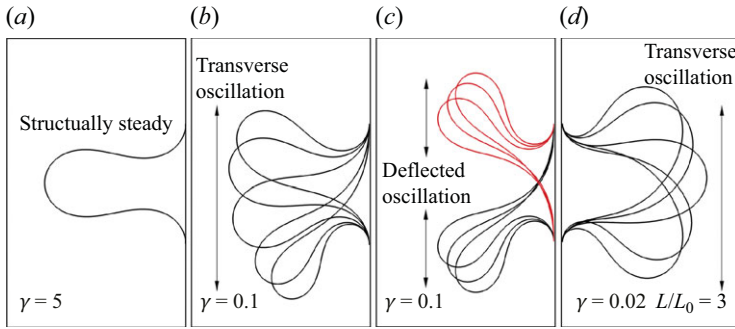


Figure 4. Superposition of the instantaneous shapes of the filament in (a) sSS mode ( $\gamma = 5$ ), (b)  $TO_i$  mode ( $\gamma = 0.1$ ), (c) DO mode ( $\gamma = 0.1$ ) under two directions and (d)  $TO_c$  mode ( $\gamma = 0.02$ ) ( $L/L_0 = 3$ ).

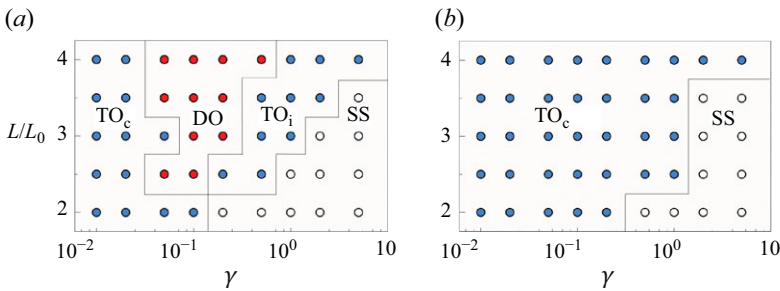


Figure 5. Mode diagram for (a) inverted and (b) conventional initial states depending on  $\gamma$  and  $L/L_0$ ; regions  $TO_c$ , DO,  $TO_i$  and SS correspond to the conventional transverse oscillation mode, the DO mode, the  $TO_i$  mode and the structurally steady mode.

inverted flags, emerges under moderate  $\gamma$  for the inverted initial state. Two types of  $TO_i$  motions manifest as  $L/L_0$  and  $\gamma$  vary: one with large-amplitude oscillations (figure 4b), occurring under conditions of moderate  $\gamma$  and high  $Re$ , and the other involving small vibrations near the structurally steady state, which appears at high  $\gamma$  close to the SS mode. In addition, the DO mode, characterized by filament deflection toward one side, is observed under moderate  $\gamma$  for the inverted initial state. Figure 4(c) illustrates two DO motions, upward DO and downward DO, based on differing initial excitations. Notably, the same filament ( $L/L_0 = 3$ ,  $\gamma = 0.1$ ) under identical conditions shows quad stability, encompassing  $TO_i$ , upward DO, downward DO and  $TO_c$  (not depicted in figure 4), depending on varying initial states. Under low  $\gamma$  values, the filament sustains  $TO_c$ , departing from the initial state, resembling the flapping motion of a conventional flag.

Here, we explore the influence of  $L/L_0$  and  $\gamma$  on the mode transition of the transversely buckled filament. The inverted initial state and conventional initial state result in distinct mode diagrams (figure 5). The inverted initial state shares a similar static divergence property with the inverted flag, rendering it more unstable than the conventional initial state, thereby leading to the emergence of the DO mode (Gurugubelli *et al.* 2015; Sader *et al.* 2016). Under low  $\gamma$  values, despite their initiation in an inverted shape, the filaments exhibit the  $TO_c$  mode because the filament is too flexible to withstand the inverted shape under fluid force, causing it to shift downstream. As  $\gamma$  increases to  $O(10^{-1})$ , the filament can sustain the inverted shape but still fails to maintain symmetry, leading to

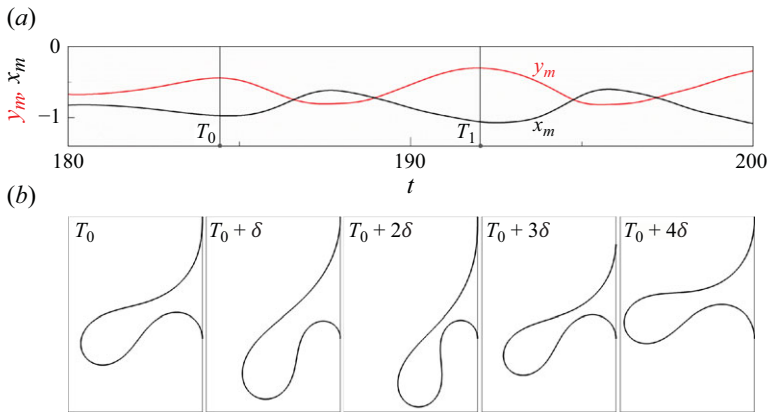


Figure 6. Time histories of (a) mid-point ( $x_m, y_m$ ) in the DO mode. (b) The sequential process of the DO mode ( $L/L_0 = 3, \gamma = 0.1$ ).

the emergence of the DO mode. As  $\gamma$  increases further, the filament shifts to a small-amplitude  $TO_i$  motion around the upstream equilibrium position. The SS mode becomes predominant at high  $\gamma$  values. Conversely, for filaments in the conventional initial state, the mode diagram is more concise, featuring the filament in the  $TO_c$  mode under low  $\gamma$  and the SS mode under high  $\gamma$ .

To elucidate the DO motion, we present the time histories of the midpoint and the sequential process in figure 6, where  $\delta$  represents one quarter of the oscillation process. In the DO mode, the filament deflects toward one side because of static divergence. At  $T_0$ ,  $y_m$  reaches its maximum value, whereas  $x_m$  reaches its minimum value, indicating the onset of a downward motion. By  $T_0 + 2\delta$ ,  $y_m$  reaches its minimum value and  $x_m$  reaches its maximum value, marking the filament's extreme position with a large deflection. The filament then commences an upward motion. At  $T_1$ , the upward motion ceases, initiating a new oscillation period. The filament displays aperiodic motion in the DO mode, a behaviour similarly observed in the deflected flapping mode of inverted flags (Gurugubelli *et al.* 2015 figure 18; Sader *et al.* 2016 figure 9).

The filament exhibits a distinctly different oscillation motion under the  $TO_c$  mode compared with that under the DO mode. Figure 7 illustrates the time histories of the midpoint and the sequential process of the  $TO_c$  mode. Observing the motion,  $y_m$  is symmetric along the  $y = 0$  axis, indicating symmetric upward and downward motion along this axis. At  $T_0$ ,  $y_m$  reaches its maximum value, whereas  $x_m$  reaches its minimum value. The filament subsequently begins its downward motion;  $y_m$  crosses the  $y = 0$  axis at  $T_0 + \delta$ , with the filament exhibiting a symmetric shape. At  $T_0 + 2\delta$ ,  $y_m$  reaches its minimum value, signifying the end of the downward motion. After  $T_0 + 2\delta$ , an upward motion commences, reversing the downward motion. Notably, the  $TO_c$  motion is completely periodic because of its more stable position compared with the inverted state. Even as  $\gamma$  decreases to 0.001, the filament does not transition to a chaotic mode but maintains periodic oscillation, differing from the behaviour of conventional flags (Argentina & Mahadevan 2005; Alben *et al.* 2008; Shelley *et al.* 2011). This stability is attributable to the presence of two clamped edges, which reinforce the filament's stability.

Here, we examine the wake pattern of the filament in different modes. Figure 8 illustrates the instantaneous contours of  $\omega_z$ , and the power spectral density (PSD) of  $v$  at ( $x = 5, y = 0$ ) for the  $TO_i$  mode, DO mode and  $TO_c$  mode. For the  $TO_i$  mode, shear layers

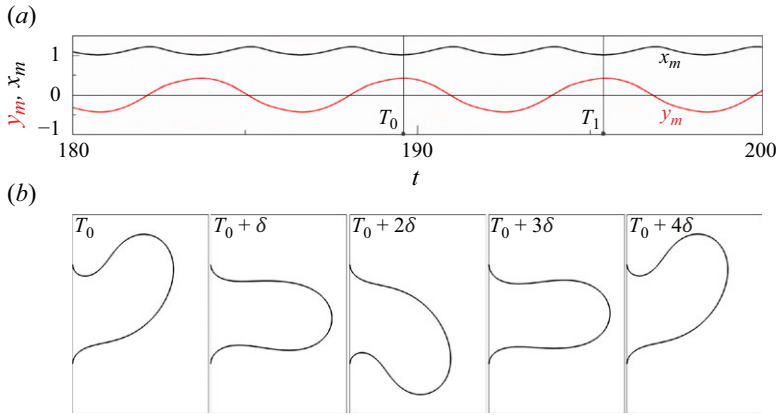


Figure 7. Time histories of (a) mid-point ( $x_m, y_m$ ) in the  $TO_c$  mode. (b) The sequential process of the  $TO_c$  mode ( $L/L_0 = 3, \gamma = 0.02$ ).

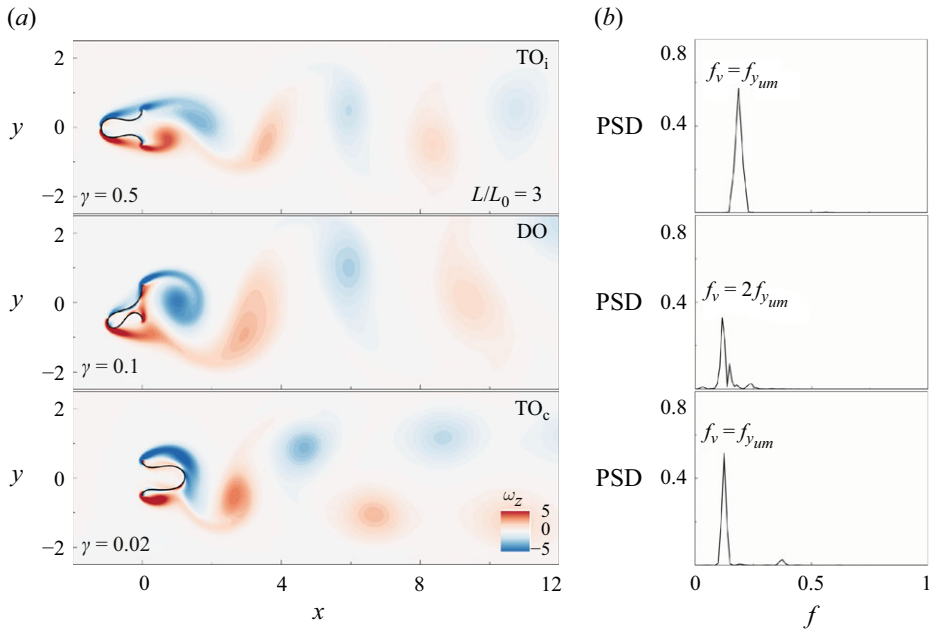


Figure 8. (a) Instantaneous contours of  $\omega_z$  and (b) PSD of  $v$  ( $x = 5, y = 0$ ) for the  $TO_i$  mode ( $\gamma = 0.5$ ), DO mode ( $\gamma = 0.1$ ) and  $TO_c$  mode ( $\gamma = 0.02$ ) under  $L/L_0 = 3$ .

form at the front part and two clamped edges. Vortices shed from the upper and lower edges, creating a symmetric 2S wake pattern. The oscillation frequency of the filament aligns with the shedding frequency of the vortices in the  $TO_i$  mode. By contrast, positive vortices form at the front part of the filament, whereas negative vortices are generated on the clamped edge opposite deflection for the DO mode. The negative vortices shed after the positive vortices, resulting in an asymmetric wake pattern termed P. The irregular PSD of  $v$  is caused by the aperiodic motion of the DO mode (figure 6). Moreover, the filament's oscillation frequency does not synchronize with the vortex shedding frequency ( $f_v > f_{y_m}$ ).

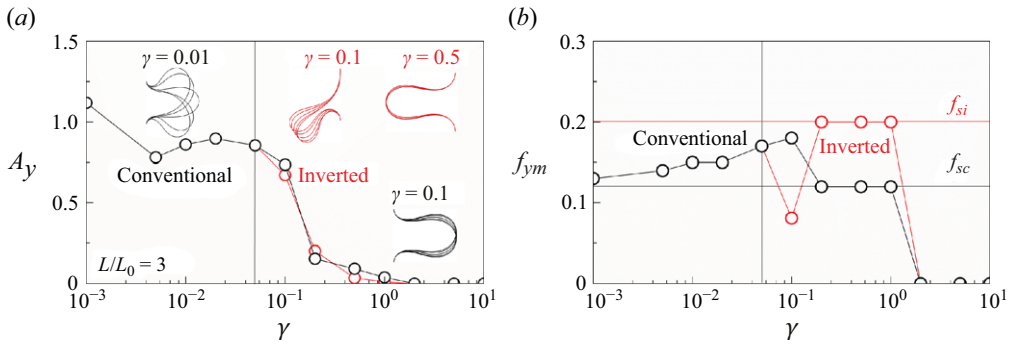


Figure 9. (a) Oscillation amplitude ( $A_y$ ) and (b) oscillation frequency ( $f_{ym}$ ) for conventional and inverted initial states as a function of  $\gamma$  ( $L/L_0 = 3$ ).

Lastly, for the filament in the  $TO_c$  mode, negative vortices form and shed from the upper clamped edges, while positive vortices form and shed from the lower clamped edge. After shedding, the positive and negative vortices align into two distinct rows, resulting in a 2S wake pattern distinct from that of the  $TO_i$  mode. The oscillation frequency of the filament also aligns with the shedding frequency of the vortices in the  $TO_c$  mode. Additional details regarding the vortex shedding for each mode will be discussed later.

### 3.2. Effects of bending rigidity

In this section, we investigate the influence of bending rigidity on the mode transition of the transverse buckled filament in a uniform flow. The ratio  $L/L_0$  is fixed at 3, ensuring that the filament is sufficiently long to display the large-amplitude oscillations characteristic of the  $TO_i$  and  $TO_c$  modes (figure 5). Figure 9 illustrates the oscillation amplitude  $A_y$  and  $f_{ym}$  for both conventional and inverted initial states (as shown in figure 4) under varying  $\gamma$ , accompanied by schematics depicting the superposition of the filament's instantaneous shapes at specific  $\gamma$  values. Here,  $f_{si}$  and  $f_{sc}$  denote the vortex shedding frequency of the corresponding rigid buckled filaments. Notably, for  $\gamma$  values below the bifurcation point (denoted by a vertical thin line in figure 9a), the filament remains in the  $TO_c$  mode irrespective of its initial configuration. Prior to the critical  $\gamma$  value being reached,  $A_y$  decreases after  $\gamma = 0.001$  and remains nearly constant thereafter, whereas  $f_{ym}$  gradually increases. In the range  $0.001 \leq \gamma \leq 0.05$ ,  $f_{ym}$  is greater than  $f_{sc}$ , indicating that the filament's oscillation is attributable to the vortices shedding. After surpassing the bifurcation point (denoted by a thin vertical line), the filament exhibits the DO mode when under the inverted initial state, whereas it remains in the  $TO_c$  mode when under the conventional state. Particularly noteworthy is the sudden decrease in  $f_{ym}$  for the filament under the DO mode ( $\gamma = 0.1$ ) and the disruption of synchronization between the filament's oscillation and vortices shedding (figure 8). Notably, the large-amplitude  $TO_i$  mode is absent in the inverted initial state. When  $\gamma$  increases to 0.2, both the conventionally and invertedly initiated filaments experience a substantial decrease in  $A_y$  and their respective  $f_{ym}$  values converge to  $f_{si}$  and  $f_{sc}$ , respectively. This behaviour indicates that  $\gamma = 0.2$  represents a critical value for  $L/L_0 = 3$ , at which the motion shifts to low-amplitude vibration for both inverted and conventional buckled filaments. When  $\gamma$  exceeds 2, the filaments shift to the SS mode for both conventional and inverted configurations. Although the filament motion is synchronous with vortex shedding for the conventional buckled filament ( $f_v = f_{ym}$ ), no obvious lock-in or resonance is observed

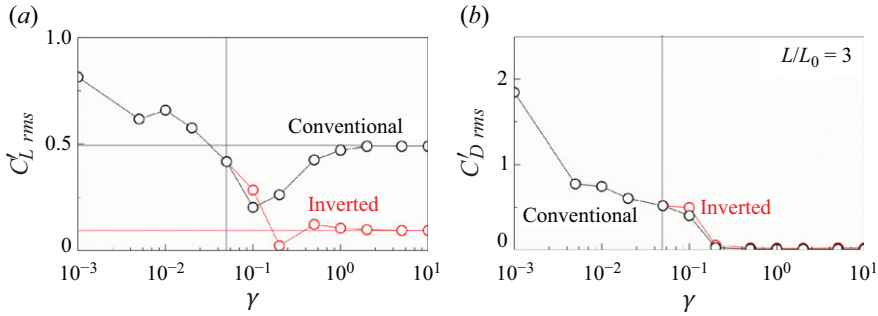


Figure 10. (a) The r.m.s. of the fluctuation lift coefficient ( $C'_{L rms}$ ) and (b) the fluctuation drag coefficient ( $C'_{D rms}$ ) for conventional and inverted buckled filaments as a function of  $\gamma$  under  $L/L_0 = 3$ .

when  $\gamma$  changes. This suggests that the  $TO_c$  mode is not a typical vortex-induced vibration, unlike the behaviour observed in elastically mounted cylinders.

To explore the effect of the fluid force applied by the surrounding flow on the filament, we investigate the root mean square (r.m.s.) of the fluctuation lift coefficient ( $C'_{L rms}$ ) and the fluctuation drag coefficient ( $C'_{D rms}$ ), as depicted in figure 10. Here, the drag coefficient ( $C_D$ ) is defined as  $f_x/0.5\rho U^2 L_0$  and the lift coefficient ( $C_L$ ) is defined as  $f_y/0.5\rho U^2 L_0$ . The drag and lift coefficients can be further decomposed into time-averaged components ( $\bar{C}_D$  and  $\bar{C}_L$ ) and fluctuation components ( $C'_D$  and  $C'_L$ ). The values  $C'_{D rms}$  and  $C'_{L rms}$  are employed to estimate the fluctuation of the fluid force, which is a primary driver of the filament's motion. The vertical black thin line denotes the bifurcation  $\gamma$  of conventional and inverted buckled filament. The horizontal black and red line represent the  $C'_{L rms}$  of the corresponding rigid buckled filament, respectively. Both  $C'_{D rms}$  and  $C'_{L rms}$  exhibit high values under low  $\gamma$ . This is caused by dramatic motion of the soft filament that leads to a peak value of fluid force as the filament reaches its extreme position. As  $\gamma$  increases, the filament motion becomes moderate, accompanied by a gradual decrease in  $C'_{D rms}$  and  $C'_{L rms}$ . After the bifurcation point, the DO mode presents with a slight decrease in  $C'_{D rms}$  and  $C'_{L rms}$ , attributed to the deflected shapes. When  $\gamma$  surpasses the critical value ( $\gamma = 0.2$ ), both  $C'_{D rms}$  and  $C'_{L rms}$  decline, attributed to the filament motion shifts to low amplitude vibration. The values of  $C'_{D rms}$  and  $C'_{L rms}$  converge to those of corresponding rigid buckled filament ( $C'_{D rms} = 0$  for rigid filament) as  $\gamma$  further increases. Additionally,  $C'_{L rms}$  of the conventional rigid filament is larger than that of the inverted one. This difference results in the conventional buckled filament being more prone to vibration compared with the inverted one under high  $\gamma$  (figure 5).

To elucidate the relationship between vortex shedding and filament motion, we analyse vorticity and pressure contours surrounding the filaments, alongside time histories of the midpoint position, fluid force, elastic force ( $F_s$ ) and energy (figure 11). We first investigate the dynamics of vortices shedding in the DO mode, examining distinct time steps denoted as A, B, C and D (illustrated in figure 11a). Corresponding contours of  $\omega_z$  and  $p$  at these specific times are displayed in figure 11(b). At time A, when  $x_m$  reaches its minimum and  $y_m$  reaches its maximum, the filament is at its extreme position, with  $E_k$  at 0. Simultaneously, a positive vortex forms at the top of the filament, whereas a negative vortex sheds from the upper clamped edge. Notably, a high-pressure zone above the filament induces its deflection. Both  $E_s$  and  $c_p$  remain at low values because filament deformation is minimal. During the transition from A to B, the filament descends under negative  $F_{fy}$ , coinciding with shedding of the positive vortex. This shedding generates a low-pressure region beneath the filament, resulting in a local minimum value of  $F_{fy}$

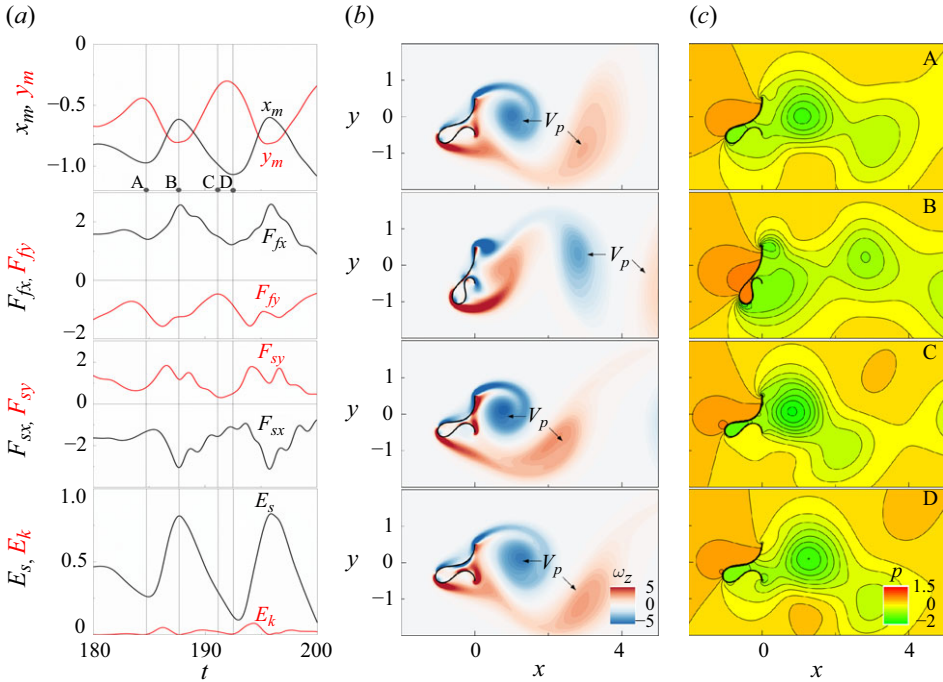


Figure 11. (a) Time histories of  $x_m$ ,  $y_m$ ,  $\mathbf{F}$  and  $E$ . Instantaneous contours of (b)  $\omega_z$  and (c)  $p$  at A, B, C and D for  $L/L_0 = 3$  and  $\gamma = 0.1$  under the DO mode.

and a local maximum value of  $F_{sy}$ . In addition,  $F_{fx}$  increases as the filament descends, characteristic of static divergence, further driving the downward motion. At time B,  $x_m$  reaches its maximum and  $y_m$  reaches its minimum, indicating the filament’s lower extreme position, with  $E_k$  at 0. The filament’s largest cross-sectional area leads to a maximum  $F_{fx}$ , whereas  $E_s$  peaks because of the large deflection. During the transition from B to C, the filament ascends, with a negative vortex shedding at the upper clamped edge. This shedding also leads to a local maximum value of  $F_{sy}$ . At time C, the shedding vortices flow downstream, causing the corresponding low-pressure field to move away from the filament, resulting in the maximum value of  $F_{fy}$ . Finally, at time D, the filament returns to its upper extreme position, concluding the DO motion. Interestingly, the choice of an initial shape with a large deflection under the same parameters results in the filament exhibiting a large-amplitude  $TO_i$  mode, resembling the bistable properties of the transition between the flapping and deflected modes observed in the inverted flag (Tang *et al.* 2015). These observations highlight that the critical factor governing both the DO mode and the large-amplitude  $TO_i$  mode is whether the filament retains sufficient elastic energy to return to its symmetric position. Our observations suggest that, because shedding downstream does not substantially affect filament motion, vortex shedding is not the primary factor in the DO mode. Instead, movement-induced variation of aerodynamic and elastic forces might play a more substantial role, indicating that the DO mode resembles a ‘galloping-type’ oscillation (Goza *et al.* 2018; Tavallaeinejad *et al.* 2020).

Shifting our focus to the vortex dynamics of the filament under the  $TO_c$  mode, figure 12 presents time histories of  $x_m$ ,  $y_m$ ,  $\mathbf{F}$  and  $E$ , synchronized with instantaneous contours of  $\omega_z$  and  $p$  at A, B, C and D. At time A, the filament reaches its upper extreme position with maximum  $y_m$ , minimum  $x_m$  and  $E_k$  at zero. A positive  $V_s$  forms at the lower clamped

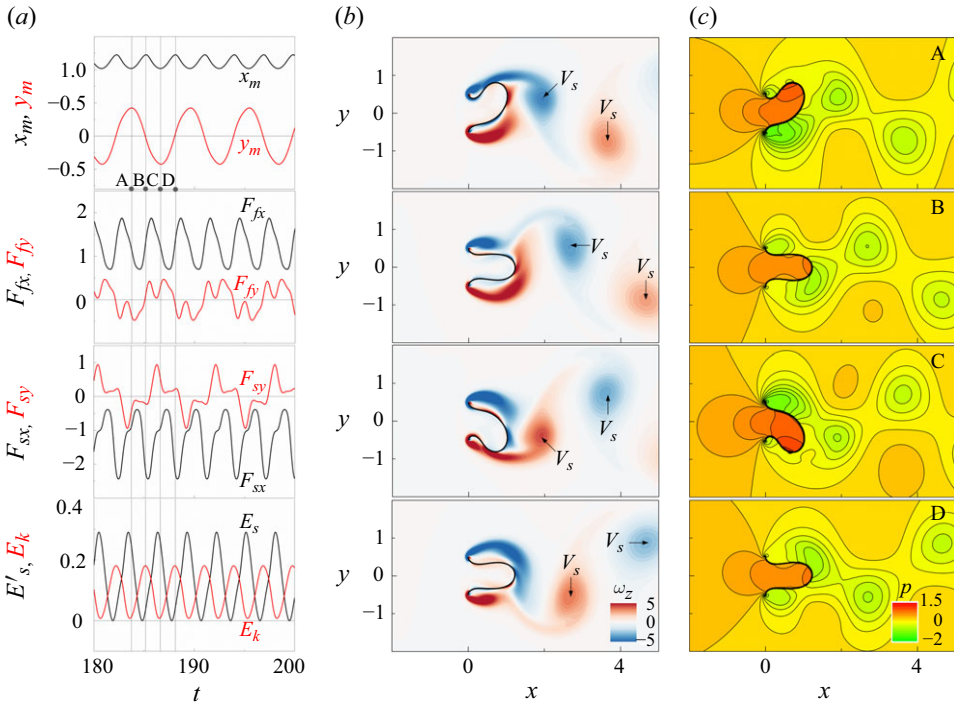


Figure 12. (a) Time histories of  $x_m$ ,  $y_m$ ,  $\mathbf{F}$ , and  $E$ . Instantaneous contours of (b)  $\omega_z$  and (c)  $p$  at A, B, C and D for  $L/L_0 = 3$  and  $\gamma = 0.05$  under the  $TO_c$  mode.

edge, inducing a low-pressure region beneath the filament and resulting in negative  $F_{fy}$ . The value of  $E_s$  peaks because of the substantial deflection of the filament. During the transition from A to B, the filament descends under negative  $F_{fy}$  and  $F_{sy}$ , accompanied by shedding of the positive  $V_s$ . By time B, the filament adopts a symmetric shape with nearly zero  $F_{fy}$  and all elastic energy is converted into kinetic energy, facilitating continued downward motion. In the period from B to C, a high-pressure region enclosed by the filament forms, leading to a reduction in  $F_{fy}$ . At time C, both  $y_m$  and  $x_m$  reach their minimum values, marking the filament's lower extreme position, with all kinetic energy converting to elastic energy, resulting in maximum  $E_s$ . A negative  $V_s$  emerges at the upper clamped edge, creating a low-pressure zone above the filament. As the filament ascends from C to D under positive  $F_{fy}$  and  $F_{sy}$ , shedding of the negative  $V_s$  occurs. By time D, the filament adopts a symmetric shape akin to point B, continuing its upward movement until it returns to its upper extreme position, completing a cycle of the  $TO_c$  mode. The filament under the  $TO_c$  mode clearly displays a more stable and periodic motion than the filament under the  $DO$  mode, which we attribute to its more stable position. In addition, vortices shed directly from the filament under the  $TO_c$  mode, resulting in larger fluctuations of the lift force (as observed in figure 10) and thereby substantially influencing the filament motion. The large-amplitude oscillation initiates rapidly when  $\gamma$  is lower than a certain threshold, and the amplitude increases as  $\gamma$  decreases, indicating that the  $TO_c$  mode is likely a self-induced oscillation. Moreover, no significant lock-in or resonance phenomena were observed as the bending rigidity varied, further confirming that the  $TO_c$  mode is not a vortex-induced vibration.

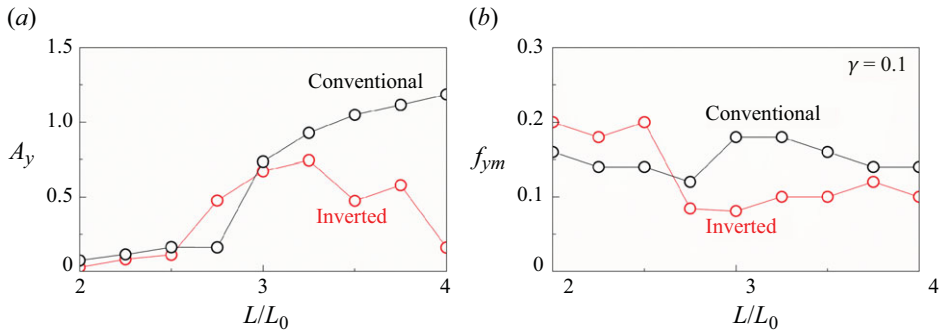


Figure 13. (a) Oscillation amplitude ( $A_y$ ) and (b) oscillation frequency ( $f_{ym}$ ) for conventional and inverted buckled filament as a function of  $L/L_0$  ( $\gamma = 0.1$ ).

### 3.3. Effects of filament length

In this section, we explore the influence of  $L/L_0$  on the filament's motion. Based on the results of § 3.2, we fixed  $\gamma$  at 0.1 to ensure that both conventional and inverted filaments exhibit large amplitude  $TO_i$  and  $TO_c$  modes across a wide range of  $L/L_0$ . Figure 13 shows  $A_y$  and  $f_{ym}$  for conventional and inverted buckled filaments as a function of  $L/L_0$  under  $\gamma = 0.1$ . At low values of  $L/L_0$ , both conventional and inverted buckled filaments exhibit small-amplitude oscillations attributable to the greater stability of shorter filaments. When  $L/L_0$  exceeds 2.5,  $A_y$  of the inverted buckled filament increases, whereas  $f_{ym}$  decreases, indicating a shift from the  $TO_i$  mode to the DO mode. With further increases in  $L/L_0$  to 3, both  $A_y$  and  $f_{ym}$  increase for the conventional buckled filament, signifying a transition from low-amplitude vibration to large-amplitude oscillation. As  $L/L_0$  continues to rise,  $A_y$  of the inverted buckled filament decreases, whereas that of the conventional buckled filament continues to increase. This tendency is attributed to the long filament bending more than 90 degrees, where streamwise motion dominates, resulting in a decrease in  $A_y$ . Conversely, the conventional buckled filament retains the  $TO_c$  mode as  $L/L_0$  increases, accompanied by decreases in  $f_{ym}$ .

We used instantaneous vorticity contours and the time history of  $F_f$  to elucidate the effect of  $L/L_0$  on filament motion for the inverted buckled filament, as depicted in figure 14. For a short filament ( $L/L_0 = 2$ ), the wake exhibits a symmetric von Kármán vortex street, resulting in sinusoidal  $F_{fx}$  and  $F_{fy}$ . The filament displays minor vibration due to the low-amplitude variation of  $F_f$ . When  $L/L_0$  increases to 3, the filament transitions to the DO mode, accompanied by an asymmetric wake pattern. Both  $F_{fx}$  and  $F_{fy}$  exhibit substantial variation that is notably greater than that of the filament under  $L/L_0 = 2$ , leading to an increase in  $A_y$  of the inverted buckled filament (figure 13a). The deflection of the filament intensifies when  $L/L_0 = 4$ . Importantly, the variation of  $F_{fx}$  exceeds that of  $F_{fy}$ , suggesting that motion in the  $x$ -direction is dominant, resulting in a decrease in  $A_y$  (figure 13a).

### 3.4. Effects of Reynolds number

The parameter  $Re$  plays an important role in the motion of buckled filaments. In this section, we examine the effect of  $Re$  on both conventional and inverted buckled filaments. For this analysis, we fix the parameters  $\gamma$  and  $L/L_0$  at moderate values of

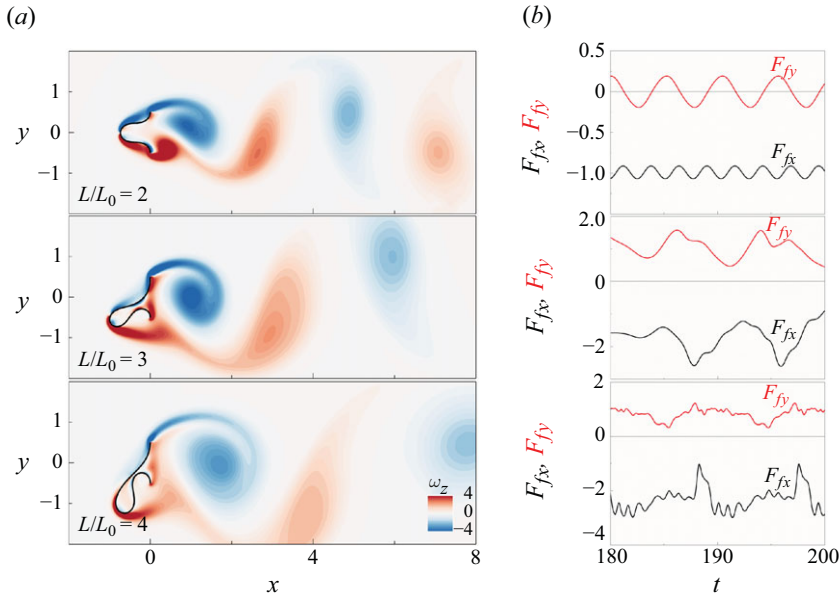


Figure 14. (a) Instantaneous contours of  $\omega_z$  and (b) time histories of  $F_f$  for inverted buckled filament under  $L/L_0 = 2, 3, 4$  ( $\gamma = 0.1$ ).

0.1 and 3, respectively. Figure 15 shows the amplitude of  $A_y$  and  $f_{ym}$  for both inverted and conventional buckled filaments as  $Re$  is varied. At  $Re = 50$ , both types of filaments exhibit a small  $A_y$ . When  $Re$  increases to 100,  $A_y$  increases for both filaments. This increase is attributed to the transition of the inverted buckled filament from a small-amplitude to a large-amplitude DO mode and the conventional buckled filament to a  $TO_c$  mode. When  $Re$  surpasses 150, the inverted buckled filament exhibits a large-amplitude  $TO_i$  mode (as shown in figure 5b). This large-amplitude  $TO_i$  mode is absent at low  $Re$ , similar to the absence of flapping mode at low  $Re$  for inverted flags (Goza *et al.* 2018). As  $Re$  increases further,  $A_y$  for both inverted and conventional buckled filaments stabilize, whereas  $f_{ym}$  for the inverted buckled filament decreases. Interestingly,  $f_{ym}$  remains constant as  $Re$  increases for the conventional buckled filament. This constancy aligns with the conventional buckled filament's vortex shedding frequency. The Strouhal number ( $St$ ), defined as  $f_{vs}L_0/U_0$ , remains  $\sim 0.2$  for the conventional buckled filament and is insensitive to variations of  $Re$ .

To clearly demonstrate the influence of  $Re$  on filament motion, figure 16 shows the time histories of the midpoint ( $x_m, y_m$ ) for both inverted and conventional buckled filaments under different  $Re$  values. At  $Re = 50$ , the inverted buckled filament is in a small-amplitude DO mode, indicated by a non-zero mean  $y_m$  value, whereas the conventional buckled filament remains in a near-equilibrium state. As  $Re$  increases to 200, the inverted buckled filament transitions to a  $TO_i$  mode, exhibiting periodic upward and downward oscillations similar to the flapping mode of an inverted flag. Conversely, the conventional buckled filament shifts to a  $TO_c$  mode, characterized by a high oscillation frequency and a relatively lower amplitude. At  $Re = 300$ , the inverted buckled filament maintains large-amplitude oscillations, although the periodicity begins to break down. The conventional buckled filament displays similar behaviour at  $Re = 300$  as it did at  $Re = 200$ , suggesting that the  $TO_c$  mode is insensitive to changes in  $Re$ . When  $Re$  is

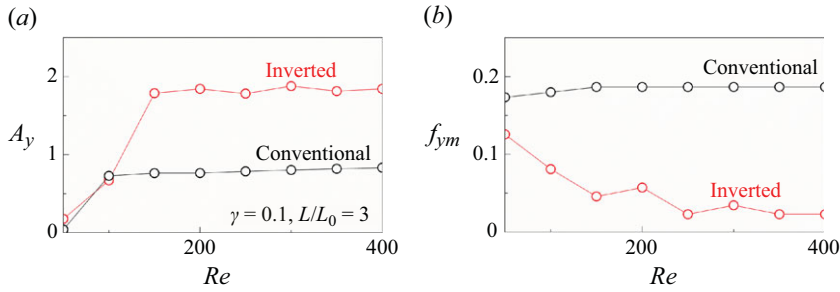


Figure 15. (a) Oscillation amplitude ( $A_y$ ) and (b) oscillation frequency ( $f_{y_m}$ ) for conventional and inverted buckled filament as a function of  $Re$  ( $\gamma = 0.1, L/L_0 = 3$ ).

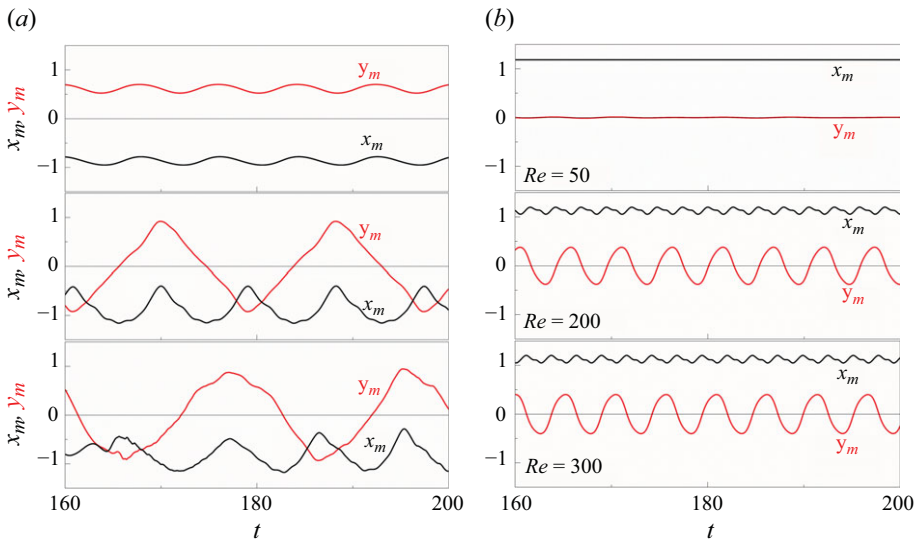


Figure 16. Time histories of mid-point ( $x_m, y_m$ ) for (a) inverted and (b) conventional buckled filament under different  $Re$  ( $\gamma = 0.1, L/L_0 = 3$ ).

increased further, the inverted buckled filament exhibits irregular motion, whereas the conventional buckled filament continues to oscillate regularly. These observations indicate that  $Re$  strongly influences the mode transition of the inverted buckled filament. By contrast, the conventional buckled filament shows less sensitivity to changes in  $Re$  than the inverted filament.

Here, we analyse the interaction between shedding vortices and the motion of the filament in the large-amplitude  $TO_i$  mode. Figure 17 shows the instantaneous vorticity and pressure contours, along with the time histories of the midpoint position, fluid force, elastic force and energy over one half of a transverse oscillation period. The filament in the large-amplitude  $TO_i$  mode displays a ‘2S + 2P’ wake pattern, distinct from the low-amplitude  $TO_i$  mode and the DO mode. At time A, the filament is at its upper extreme position, identified by the maximum values of  $y_m$  and  $x_m$ . Concurrently,  $E_s$  also reaches its peak because of the substantial deflection. A negative  $V_s$  forms at the upper clamped edge, and a  $V_p$  forms at the lower clamped edge. Notably, a high-pressure region enclosed

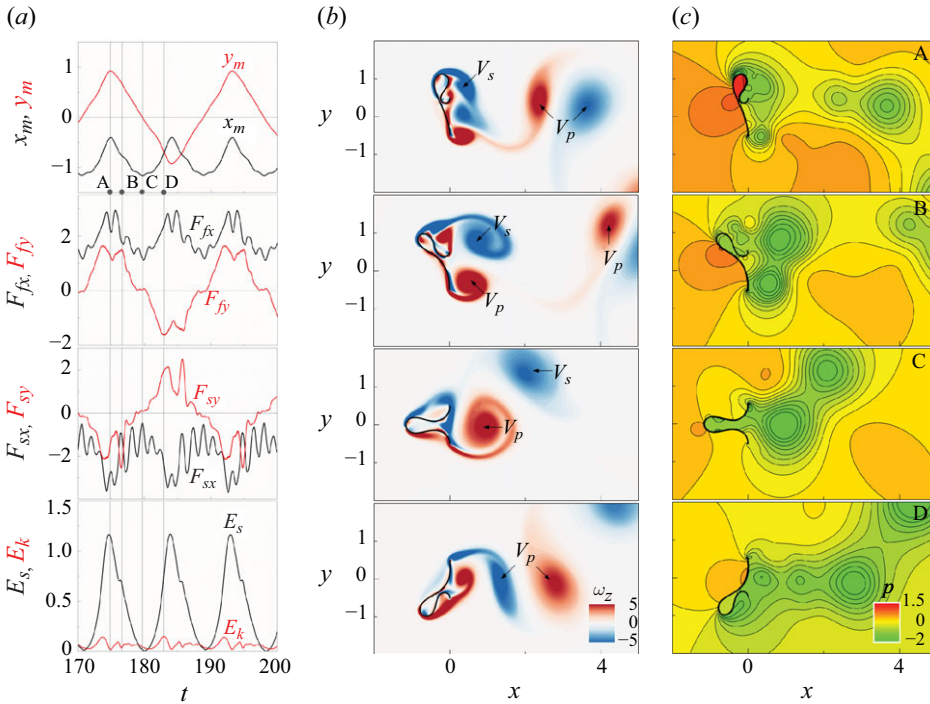


Figure 17. (a) Time histories of  $x_m$ ,  $y_m$ ,  $\mathbf{F}$  and  $E$ . Instantaneous contours of (b)  $\omega_z$  and (c)  $p$  at A, B, C and D for  $Re = 200$  under the large-amplitude  $TO_i$  mode ( $\gamma = 0.1$ ,  $L/L_0 = 3$ ).

by the filament develops, causing a local decrease in  $F_{fx}$  and  $F_{fy}$ . From A to B, the filament initiates a downward motion driven by a large negative  $F_{sy}$ , with the shedding of the negative  $V_s$  and positive  $V_p$ . The high-pressure region enclosed by the filament dissipates, resulting in an increase in  $F_{fy}$ . During the transition from B to C, the filament continues to descend, with a decrease in  $F_{fy}$  and an increase in  $F_{sy}$ . At time C, the filament exhibits a symmetric shape, where  $y_m$  reaches zero. Both  $F_{fy}$  and  $F_{sy}$  are approximately zero because of the filament's symmetric shape. The value of  $E_s$  reaches its minimum, indicating low deflection at this point. From C to D, the filament continues its downstream motion due to inertia, accompanied by the shedding of a negative  $V_p$  from the upper clamped edge, induced by the previously shed positive  $V_p$ . The value of  $F_{fy}$  decreases during this period because of the static divergence of the inverted buckled filament, contributing to the downward motion. At time D,  $E_k$  achieves its maximum value,  $F_{sy}$  reaches a local maximum and  $F_{fy}$  hits a local minimum. After time D, a high-pressure region forms in the closure area, leading to an increase in  $F_{fy}$  and a decrease in  $F_{sy}$ . When the filament reaches its lower extreme position, the downward motion ceases and a symmetric upward motion begins. Indeed, we note that the fluid force is higher for  $Re = 200$  than for  $Re = 100$ , which results in a larger deflection of the filament, enabling it to store more elastic energy. Consequently, the filament can return to its symmetric position after reaching its lower/upper extreme position, thereby contributing to the manifestation of the large-amplitude  $TO_i$  mode. On the basis of this analysis, the filament's motion does not synchronize with the vortex shedding frequency ( $f_v = 3f_{y_m} = 0.16$ ), suggesting that vortex shedding might not be the primary driver of the large-amplitude  $TO_i$  mode. Instead, the interplay between destabilizing fluid forces and stabilizing elastic forces likely governs the dynamics of the  $TO_i$  mode.

### 3.5. Energy-harvesting performance

A dimensional analysis of the energy equations is employed to further evaluate the contribution of each component on energy-harvesting performance. The term  $K$  in (2.15) represents the curvature of the filament. By applying a Fourier transform to both sides of (2.15), we derive the energy equation in the frequency domain

$$(i\beta_e\omega + 1)\hat{V} = -i\alpha_e\beta_e\omega\sqrt{\gamma}K, \tag{3.1}$$

where  $\omega = 2\pi f_{ym}$  represents the dominant angular frequency of the filament,  $\hat{V}$  is the amplitude,  $\gamma$  denotes the bending rigidity,  $K$  is the local curvature of the filament and  $\alpha_e$  and  $\beta_e$  are the coupling coefficient and the tuning coefficient of the electrical system, respectively. By combining Parseval's theorem with (3.1), the mean power coefficient  $\bar{c}_p$  can be estimated by

$$\bar{c}_p \sim \frac{1}{\beta_e} \int_0^1 \hat{V}^2 ds \sim \frac{1}{\beta_e} \frac{(\beta_e\omega)^2}{(\beta_e\omega)^2 + 1} \gamma \alpha_e^2 K^2. \tag{3.2}$$

Given the small value of  $\beta_e$  used in this study, the expression simplifies to

$$\bar{c}_p \sim \gamma \beta_e \alpha_e^2 \omega^2 K^2. \tag{3.3}$$

From this analysis, we can directly assess the influence of bending rigidity, oscillation frequency and filament deformation on energy harvesting. The deformation and oscillation frequency are particularly significant, as  $\bar{c}_p$  is proportional to the square of curvature, indicating that the motion combine high frequency and large deflection is beneficial to energy harvesting. Although  $\bar{c}_p$  is only linearly proportional to  $\gamma$ , the activation range of  $\gamma$  spans several magnitudes closely impacting  $\bar{c}_p$ .

Finally, we assess the energy-harvesting performance of both inverted and conventional buckled filaments, using a streamwise configuration for comparison. Because of the presence of clamped edges, the buckled filament possesses considerable elastic energy in its initial shape. Therefore, we use the available time-averaged elastic energy ( $\bar{E}'_s = \bar{E}_s - \bar{E}_{s\ min}$ ) and power coefficient ( $\bar{c}'_p = \bar{c}_p - \bar{c}_{p\ min}$ ) to evaluate the harvested energy during filament motion. Figure 18 illustrates  $\bar{E}'_s$  and  $\bar{c}'_p$  for both conventional and inverted buckled filaments as a function of  $\gamma$ . All configurations exhibit relatively low  $\bar{E}'_s$  and  $\bar{c}'_p$  values under low  $\gamma$ . As  $\gamma$  increases, both  $\bar{E}'_s$  and  $\bar{c}'_p$  gradually increase because they are functions of  $\gamma$ . When  $\gamma$  surpasses 0.012, the streamwise-clamped filament transitions from the STO mode to the streamwise oscillation mode, leading to a sudden decrease in  $\bar{E}'_s$  and  $\bar{c}'_p$  (Mao *et al.* 2023). As  $\gamma$  increases to 0.02, the  $\bar{c}'_p$  of both conventional and inverted buckled filaments reaches its maximum value. At  $\gamma = 0.1$ , the DO mode emerges, exhibiting substantial  $\bar{E}'_s$  value because of its large-amplitude deflection. In contrast, the  $\bar{c}'_p$  in the DO mode is lower than that of 0.02 due to the reduced oscillation amplitude. Both inverted and conventional buckled filaments transition to low-amplitude oscillation at  $\gamma = 0.2$ , resulting in a decrease in  $\bar{E}'_s$  and  $\bar{c}'_p$ . As  $\gamma$  increases further, both configurations eventually stabilize, causing  $\bar{E}'_s$  and  $\bar{c}'_p$  to decrease to 0. From this analysis, the transversely clamped filament demonstrates superior energy-harvesting performance across most values of  $\gamma$  compared with the streamwise configuration. This improvement is driven by the higher oscillation frequency and greater critical bending rigidity of the transversely clamped setup.

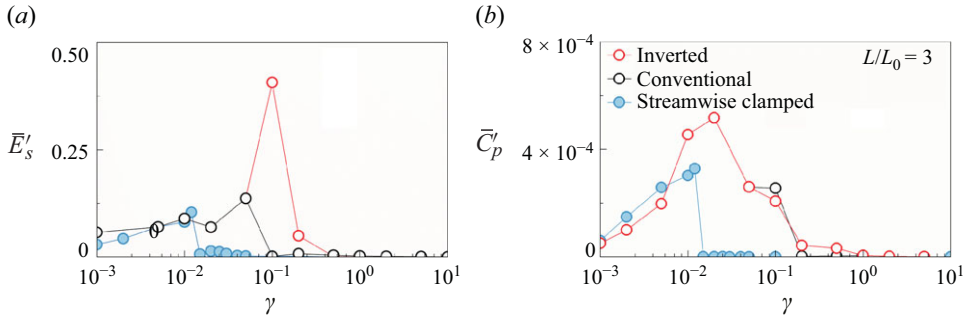


Figure 18. Values of (a)  $\bar{E}'_s$  and (b)  $\bar{c}'_p$  for conventional and (b) inverted buckled filaments as a function of  $\gamma$  under  $L/L_0 = 3$ . The results are compared with those for a streamwise-clamped (snap-through) buckled filament.

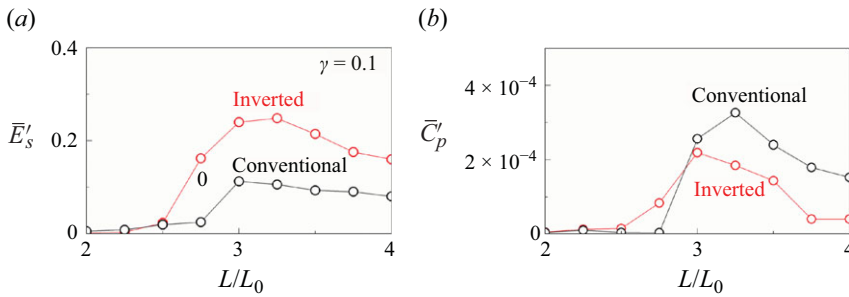


Figure 19. Values of (a)  $\bar{E}'_s$  and (b)  $\bar{c}'_p$  for conventional and (b) inverted buckled filaments as a function of  $L/L_0$  ( $\gamma = 0.1$ ).

Figure 19 depicts the influence of  $L/L_0$  on  $\bar{E}'_s$  and  $\bar{c}'_p$  for both inverted and conventional buckled filaments. At  $L/L_0 = 2$ , both configurations exhibit low values of  $\bar{E}'_s$  and  $\bar{c}'_p$ , which are attributed to the low-amplitude vibration. As  $L/L_0$  surpasses 2.5, the inverted buckled filament transitions from the small-amplitude  $TO_i$  mode to the DO mode, resulting in a significant increase in  $\bar{E}'_s$  and  $\bar{c}'_p$  due to the large deflection characteristic of the DO mode. As  $L/L_0$  continues to increase, both  $\bar{E}'_s$  and  $\bar{c}'_p$  decline for the inverted filament, which is attributed to a reduction in oscillation amplitude (figure 13). In contrast, when  $L/L_0$  reaches 3, the conventional buckled filament enters the large amplitude  $TO_c$  mode, leading to an increase in  $\bar{E}'_s$  and  $\bar{c}'_p$ . Further increases in  $L/L_0$  cause  $\bar{E}'_s$  and  $\bar{c}'_p$  to decrease, due to a reduction in oscillation amplitude and frequency. The inverted buckled filament achieves higher  $\bar{E}'_s$  due to its large deflections in the DO mode, while the conventional buckled filament demonstrates higher  $\bar{c}'_p$ , driven by its higher oscillation frequency.

The parameter  $Re$  also influences the energy-harvesting performance. Figure 20 illustrates  $\bar{E}'_s$  and  $\bar{c}'_p$  for the inverted and conventional buckled filaments as  $Re$  varies. At  $Re = 50$ , both inverted and conventional buckled filaments exhibit low values of  $\bar{E}'_s$  and  $\bar{c}'_p$ , which is attributed to their low oscillation amplitudes. As  $Re$  increases to 100, the inverted buckled filament transitions to a large-amplitude oscillation, whereas the conventional buckled filament switches to a  $TO_c$  mode, resulting in an increase in  $\bar{E}'_s$  and  $\bar{c}'_p$ . As  $Re$  increases further, the inverted buckled filament maintains its

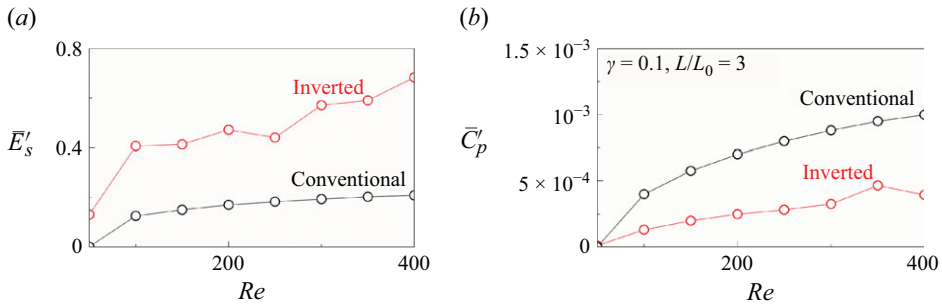


Figure 20. Values of (a)  $\bar{E}'_s$  and (b)  $\bar{c}'_p$  for the inverted and (b) conventional buckled filaments as a function of  $Re(m_1 = 0.1, L/L_0 = 3)$ .

TO<sub>i</sub> motion, leading to a continuous increase in  $\bar{E}'_s$  and  $\bar{c}'_p$ . In contrast, the values for the conventional buckled filament increase with  $Re$ . The higher  $\bar{c}'_p$  of the conventional buckled filament can be attributed to its increased oscillation frequency, as shown in figure 15.

#### 4. Conclusions

We investigated the flow-induced oscillation of transversely clamped buckled flexible filaments using the penalty IB method. The transversely clamped buckled filament can be categorized as either an inverted buckled filament or a conventional buckled filament on the basis of its position. Four distinct modes were identified for both the inverted and conventional initial conditions as  $\gamma$  and  $Re$  varied: the TO<sub>c</sub> mode, the TO<sub>i</sub> mode, the DO mode and the SS mode. At a low  $\gamma$ , the filament converges to the TO<sub>c</sub> mode irrespective of its initial shape because it cannot resist the streamwise fluid force. The TO<sub>c</sub> mode resembles the flapping mode of a conventional flag, excited by unsteady fluid forces generated by the 2S wake pattern. When  $\gamma$  increases to a bifurcation point, the inverted buckled filament can maintain its shape against the incoming flow, leading to the DO mode. The DO mode is characterized by the large deflection but low oscillation frequency motion with a ‘P’ wake pattern. The TO<sub>i</sub> mode resembles the flapping mode of an inverted flag, with small- and large-amplitude TO<sub>i</sub> modes identified, exhibiting ‘2S’ and ‘2S + 2P’ wake patterns, respectively. Multistability was observed around  $\gamma = 0.1$ , with filaments shifting to the TO<sub>c</sub> mode, TO<sub>i</sub> mode or DO mode on the basis of their initial conditions. Both inverted and conventional buckled filaments sustain the SS mode when  $\gamma$  is sufficiently high. When  $L/L_0$  increases to around 3, the filaments initiate large-amplitude oscillations. For the inverted buckled filament, the deflection of the filament in the DO mode becomes larger and the streamwise motion gradually dominates as  $L/L_0$  increases. By contrast, the oscillation amplitude increases with increasing  $L/L_0$  for the conventional buckled filament. The parameter  $Re$  plays an important role in the behaviour of the inverted buckled filament, with larger  $Re$  values contributing to the presence of the large-amplitude TO<sub>i</sub> mode. Conversely, the conventional buckled filament is almost insensitive to  $Re$  under moderate  $\gamma$ . Finally, we estimated the energy-harvesting performance by considering the elastic energy and power coefficient. Transversely clamped buckled filaments exhibit better energy-harvesting performance than streamwise-clamped buckled filaments. Our investigation of the basic configurations of a transversely clamped buckled flexible filament provides important insights into advanced flow-induced applications in energy harvesting.

**Funding.** This study was supported by a grant from the National Research Foundation of Korea (no. 2019M3C1B7025091).

**Declaration of interests.** The authors report no conflict of interest.

REFERENCES

- ALBEN, S. & SHELLEY, M.J. 2008 Flapping states of a flag in an inviscid fluid: bistability and the transition to chaos. *Phys. Rev. Lett.* **100** (7), 074301.
- ARGENTINA, M. & MAHADEVAN, L. 2005 Fluid-flow-induced flutter of a flag. *Proc. Natl Acad. Sci. USA* **102** (6), 1829–1834.
- BAI, Q., LIAO, X.-W., CHEN, Z.-W., GAN, C.-Z., ZOU, H.-X., WEI, K.-X., GU, Z. & ZHENG, X.-J. 2022 Snap-through triboelectric nanogenerator with magnetic coupling buckled bistable mechanism for harvesting rotational energy. *Nano Energy* **96**, 107118.
- BANERJEE, S., CONNELL, B.S.H. & YUE, D.K.P. 2015 Three-dimensional effects on flag flapping dynamics. *J. Fluid Mech.* **783**, 103–136.
- CHEN, Y., RYU, J., LIU, Y. & SUNG, H.J. 2020a Flapping dynamics of vertically clamped three-dimensional flexible flags in a poiseuille flow. *Phys. Fluids* **32** (7), 071905.
- CHEN, Y., YANG, J., LIU, Y. & SUNG, H.J. 2020b Heat transfer enhancement in a poiseuille channel flow by using multiple wall-mounted flexible flags. *Intl J. Heat Mass Transfer* **163**, 120447.
- CHEN, Z., LIU, Y. & SUNG, H.J. 2024 Snap-through dynamics of buckled flexible filaments in a side-by-side configuration. *Intl J. Heat Fluid Flow* **107**, 109417.
- CHEN, Z., MAO, Q., LIU, Y. & SUNG, H.J. 2023 Snap-through dynamics of a buckled flexible filament with different edge conditions. *Phys. Fluids* **35** (10), 103602.
- CHEN, Z., MAO, Q., LIU, Y. & SUNG, H.J. 2024 Snap-through dynamics of a buckled flexible filament in a channel flow. *Phys. Fluids* **36** (1), 013610.
- CISONNI, J., LUCEY, A.D., ELLIOTT, N.S.J. & HEIL, M. 2017 The stability of a flexible cantilever in viscous channel flow. *J. Sound Vib.* **396**, 186–202.
- COTTONE, F., GAMMAITONI, L., VOCCA, H., FERRARI, M. & FERRARI, V. 2012 Piezoelectric buckled beams for random vibration energy harvesting. *Smart Mater. Struct.* **21** (3), 035021.
- DOARÉ, O. & MICHELIN, S. 2011 Piezoelectric coupling in energy-harvesting fluttering flexible plates: linear stability analysis and conversion efficiency. *J. Fluids Struct.* **27** (8), 1357–1375.
- ELOY, C., LAGRANGE, R., SOUILLIEZ, C. & SCHOUVEILER, L. 2008 Aeroelastic instability of cantilevered flexible plates in uniform flow. *J. Fluid Mech.* **611**, 97–106.
- GOLDSTEIN, D., HANDLER, R. & SIROVICH, L. 1993 Modeling a no-slip flow boundary with an external force field. *J. Comput. Phys.* **105** (2), 354–366.
- GOMEZ, M., MOULTON, D.E. & VELLA, D. 2017a Passive control of viscous flow via elastic snap-through. *Phys. Rev. Lett.* **119** (14), 144502.
- GOMEZ, M., MOULTON, D.E. & VELLA, D. 2017b Critical slowing down in purely elastic snap-through instabilities. *Nat. Phys.* **13** (2), 142–145.
- GOZA, A., COLONIUS, T. & SADER, J.E. 2018 Global modes and nonlinear analysis of inverted-flag flapping. *J. Fluid Mech.* **857**, 312–344.
- GURUGUBELLI, P.S. & JAIMAN, R.K. 2015 Self-induced flapping dynamics of a flexible inverted foil in a uniform flow. *J. Fluid Mech.* **781**, 657–694.
- GURUGUBELLI, P.S. & JAIMAN, R.K. 2019 Large amplitude flapping of an inverted elastic foil in uniform flow with spanwise periodicity. *J. Fluids Struct.* **90**, 139–163.
- HUANG, W.-X., CHANG, C.B. & SUNG, H.J. 2011 An improved penalty immersed boundary method for fluid-flexible body interaction. *J. Comput. Phys.* **230** (12), 5061–5079.
- HUANG, W.-X., SHIN, S.J. & SUNG, H.J. 2007 Simulation of flexible filaments in a uniform flow by the immersed boundary method. *J. Comput. Phys.* **226** (2), 2206–2228.
- HUANG, W.-X. & SUNG, H.J. 2007 Vortex shedding from a circular cylinder near a moving wall. *J. Fluids Struct.* **23** (7), 1064–1076.
- HUANG, W.-X. & SUNG, H.J. 2010 Three-dimensional simulation of a flapping flag in a uniform flow. *J. Fluid Mech.* **653**, 301–336.
- JUNG, S.-M. & YUN, K.-S. 2010 Energy-harvesting device with mechanical frequency-up conversion mechanism for increased power efficiency and wideband operation. *Appl. Phys. Lett.* **96** (11), 111906.
- KIM, D., COSSÉ, J., HUERTAS CERDEIRA, C. & GHARIB, M. 2013 Flapping dynamics of an inverted flag. *J. Fluid Mech.* **736**, R1.
- KIM, H., LAHOOTI, M., KIM, J. & KIM, D. 2021 Flow-induced periodic snap-through dynamics. *J. Fluid Mech.* **913**, A52.

- KIM, H., ZHOU, Q., KIM, D. & OH, I.-K. 2020 Flow-induced snap-through triboelectric nanogenerator. *Nano Energy* **68**, 104379.
- KIM, J., KIM, H. & KIM, D. 2021 Snap-through oscillations of tandem elastic sheets in uniform flow. *J. Fluids Struct.* **103**, 103283.
- KIM, K., BAEK, S.-J. & SUNG, H.J. 2002 An implicit velocity decoupling procedure for the incompressible navier-stokes equations. *Intl J. Numer. Meth. Fluids* **38** (2), 125–138.
- KIM, S.Y., SUNG, H.J. & HYUN, J.M. 1992 Mixed convection from multiple-layered boards with cross-streamwise periodic boundary conditions. *Intl J. Heat Mass Transfer* **35** (11), 2941–2952.
- LEE, J.B., PARK, S.G., KIM, B., RYU, J. & SUNG, H.J. 2017 Heat transfer enhancement by flexible flags clamped vertically in a poiseuille channel flow. *Intl J. Heat Mass Transfer* **107**, 391–402.
- LEE, J.B., PARK, S.G. & SUNG, H.J. 2018 Heat transfer enhancement by asymmetrically clamped flexible flags in a channel flow. *Intl J. Heat Mass Transfer* **116**, 1003–1015.
- MAO, Q., LIU, Y. & SUNG, H.J. 2023 Snap-through dynamics of a buckled flexible filament in a uniform flow. *J. Fluid Mech.* **969**, A33.
- MICHELIN, S. & DOARÉ, O. 2013 Energy harvesting efficiency of piezoelectric flags in axial flows. *J. Fluid Mech.* **714**, 489–504.
- MICHELIN, S., LLEWELLYN SMITH, S.G. & GLOVER, B.J. 2008 Vortex shedding model of a flapping flag. *J. Fluid Mech.* **617**, 1–10.
- ORREGO, S., SHOELE, K., RUAS, A., DORAN, K., CAGGIANO, B., MITTAL, R. & KANG, S.H. 2017 Harvesting ambient wind energy with an inverted piezoelectric flag. *Appl. Energy* **194**, 212–222.
- PARK, J.W., RYU, J. & SUNG, H.J. 2019 Effects of the shape of an inverted flag on its flapping dynamics. *Phys. Fluids* **31** (2), 021904.
- PARK, S.G. 2020 Heat transfer enhancement by a wall-mounted flexible vortex generator with an inclination angle. *Intl J. Heat Mass Transfer* **148**, 119053.
- PARK, S.G., KIM, B., CHANG, C.B., RYU, J. & SUNG, H.J. 2016 Enhancement of heat transfer by a self-oscillating inverted flag in a poiseuille channel flow. *Intl J. Heat Mass Transfer* **96**, 362–370.
- RYU, J., PARK, S.G., KIM, B. & SUNG, H.J. 2015 Flapping dynamics of an inverted flag in a uniform flow. *J. Fluids Struct.* **57**, 159–169.
- SADER, J.E., COSSÉ, J., KIM, D., FAN, B. & GHARIB, M. 2016 Large-amplitude flapping of an inverted flag in a uniform steady flow – a vortex-induced vibration. *J. Fluid Mech.* **793**, 524–555.
- SADER, JOHN E., HUERTAS-CERDEIRA, C. & GHARIB, M. 2016 Stability of slender inverted flags and rods in uniform steady flow. *J. Fluid Mech.* **809**, 873–894.
- SHELLEY, M., VANDENBERGHE, N. & ZHANG, J. 2005 Heavy flags undergo spontaneous oscillations in flowing water. *Phys. Rev. Lett.* **94** (9), 094302.
- SHELLEY, M.J. & ZHANG, J. 2011 Flapping and bending bodies interacting with fluid flows. *Annu. Rev. Fluid Mech.* **43** (1), 449–465.
- SHIN, S.J., HUANG, W.-X. & SUNG, H.J. 2008 Assessment of regularized delta functions and feedback forcing schemes for an immersed boundary method. *Intl J. Numer. Meth. Fluids* **58** (3), 263–286.
- SHOELE, K. & MITTAL, R. 2016 Energy harvesting by flow-induced flutter in a simple model of an inverted piezoelectric flag. *J. Fluid Mech.* **790**, 582–606.
- TANG, C., LIU, N.-S. & LU, X.-Y. 2015 Dynamics of an inverted flexible plate in a uniform flow. *Phys. Fluids* **27** (7), 073601.
- TAVALLAEINEJAD, M., PAÏDOUSSIS, M.P., FLORES SALINAS, M., LEGRAND, M., KHEIRI, M. & BOTEZ, R.M. 2020 Flapping of heavy inverted flags: a fluid-elastic instability. *J. Fluid Mech.* **904**, R5.
- XIA, Y., MICHELIN, S. & DOARÉ, O. 2015 Fluid-solid-electric lock-in of energy-harvesting piezoelectric flags. *Phys. Rev. Appl.* **3** (1), 014009.
- YU, Y. & LIU, Y. 2016 Energy harvesting with two parallel pinned piezoelectric membranes in fluid flow. *J. Fluids Struct.* **65**, 381–397.
- YU, Y., LIU, Y. & CHEN, Y. 2017 Vortex dynamics behind a self-oscillating inverted flag placed in a channel flow: time-resolved particle image velocimetry measurements. *Phys. Fluids* **29** (12), 125104.
- ZHANG, J., CHILDRESS, S., LIBCHABER, A. & SHELLEY, M. 2000 Flexible filaments in a flowing soap film as a model for one-dimensional flags in a two-dimensional wind. *Nature* **408** (6814), 835–839.
- ZHU, L. & PESKIN, C.S. 2003 Interaction of two flapping filaments in a flowing soap film. *Phys. Fluids* **15** (7), 1954–1960.
- ZHU, Y. & ZU, J.W. 2013 Enhanced buckled-beam piezoelectric energy harvesting using midpoint magnetic force. *Appl. Phys. Lett.* **103** (4), 041905.